Combustion and Flame 286 (2026) 114799

Contents lists available at ScienceDirect

Combustion and Flame

journal homepage: www.sciencedirect.com/journal/combustion-and-flame

Mechanism of how copper-coated nano-aluminum overcomes agglomeration and boosts air-breathing combustion of HTPB

Lei Yang [1], Erik Hagen [1], Yuxin Zhou, Keren Shi, Yuan Qin, Michael R. Zachariah *

University of California, Riverside, CA 92521, United States

ARTICLE INFO

Keywords:
Air-breathing
Aluminum nanoparticles
Counterflow
Eutectic melting
HTPB
Holography
Combustion

ABSTRACT

Aluminum nanoparticles (nAl) offer high energy density for solid fuels in air-breathing propulsion, but suffer from agglomeration and difficulty in particle lift-off. Here, we address this challenge by synthesizing copper-coated nAl (nAl@Cu) via a one-pot method and incorporating them into hydroxyl-terminated polybutadiene (HTPB) fuel. The nAl@Cu/HTPB fuel demonstrated sustained continuous regressions up to 10 wt% particle loading in air counterflow, exhibiting higher regression rates than neat HTPB and demonstrating frequent droplet ejections. High-speed digital inline holography captures the process of particle ejections from the HTPB surface, revealing that the ejections are driven by the gas-bubble bursts from HTPB pyrolysis. *In situ* TEM shows that the coated Cu promotes nanocracking of the alumina shell of nAl, allowing more rapid and complete aluminum oxidation. A one-dimensional diffusion-flame analysis further demonstrates that back diffusion of CO_2 and H_2O results in oxidative heat release from a single nAl@Cu particle sufficient to pyrolyze a volume of HTPB approximately one hundred times the nAl@Cu particle's volume, generating sufficient gaseous products to propel the particle off the surface and sustain combustion.

Novelty and significance statement

This work overcomes a persistent obstacle in the application of energetic nano-additives to air-breathing fuels, namely the inability of aluminum nanoparticles to ignite effectively and the consequent flame extinction. By revealing how nanoscale surface modification promotes particle ejection and sustained combustion without conventional oxidizers, it sets a new paradigm for metalized fuels. The findings provide both fundamental insights into particle–matrix interactions and practical significance for high-energy lightweight propulsion systems.

1. Introduction

Energy density is a key parameter for solid propellants, and one strategy to enhance it is the incorporation of energetic metal additives [1,2]. Compared to conventional undoped fuels such as hydroxyl-terminated polybutadiene (HTPB, 34 kJ·cm^{-3}) [3–5], aluminum nanoparticles (nAl, the most widely used metal additive, 84 kJ·cm^{-3}) deliver substantially higher energy density and elevate flame temperatures [1,6]. Another complementary approach to boost energy efficiency is air-breathing propulsion, in which atmospheric O_2 is used to oxidize the fuels in lieu of traditional oxidizers, like ammonium perchlorate (AP), to lighten the system [7–9]. However, during the combustion of Al/HTPB composites in air, nAl routinely agglomerates at the burning surface instead of dispersing into the flame, forming alumina-coated clumps that act as passivating, insulating layers, causing two-phase flow losses, and quenching further combustion, as shown in Fig. 1 [10]. Young et al. [11] also observed that nAl-enriched HTPB exhibited lower regression rates in an oxygen counterflow diffusion flame, and such issues of Al as HTPB additives have been observed with different oxidizers [10–14].

One possible strategy to prevent surface-agglomeration and promote propagation is to use surface-functionalized nAl, inspired by the previous studies on preventing boron aggregations in HTPB [9]. It is known that coating copper on aluminum nanoparticles (nAl@Cu) can dramatically lower their ignition temperature in air [15–17]. This transition-metal shell offers three key benefits: (1) it itself inhibits nAl coalescence on the fuel surface [17,18]; (2) reduces the ignition

* Corresponding author.
E-mail address: mrz@engr.ucr.edu (M.R. Zachariah).
[1] These co-first authors contributed equally to this work

https://doi.org/10.1016/j.combustflame.2026.114799
Received 20 August 2025; Received in revised form 13 January 2026; Accepted 14 January 2026
Available online 5 February 2026

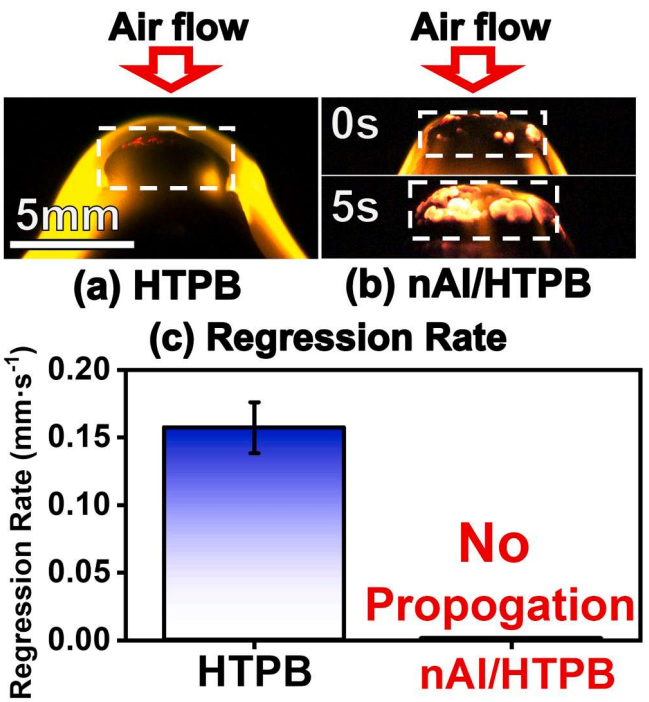

Fig. 1. (a) Continuously-burning HTPB, versus (b) flame extinction and agglomeration of nAl/HTPB (5/95wt%) in air-breathing stagnation-flow burner, where fuel grains are in white boxes; (c) regression rates of HTPB and nAl/HTPB fuel grains at T_{air}=770 K and strain rates of 100 s^{-1}.

temperature, leading to earlier heat release [15–17], which may facilitate particle detachment and ejection into gas streams; (3) the Al-Cu binary system exhibits a low-temperature eutectic melting at roughly 821 K, well below the 933 K melting point of pure aluminum [16,17,19], thus the early melting may disrupt the native alumina shell via thermal expansion and cracking, exposing fresh Al surface for rapid and complete oxidations [16].

A comprehensive study on air-breathing fuels is challenging due to the complex interactions between the diffusion-flame fluid dynamics with heat and mass transfer on the fuel surface [20]. The stagnation-flow configuration offers an effective approach for coupling the combustion process and regression rates of solid fuels, as it simplifies the system to a quasi-one-dimensional configuration [20–24]. Furthermore, high-speed imaging diagnostics with infrared cameras [25,26], digital inline holography (DIH) [27], and three-color pyrometry [28,29], when incorporated with the counterflow burner, allow real-time tracking of the ejected particles with spatial and thermal resolution.

In this study, we demonstrate that nAl@Cu particles can sustain steady air-breathing combustion in HTPB, avoiding the formation of the alumina clumps on the burning surface. The HTPB fuel with nAl@Cu (up to 10 wt% particle loading) reaches higher regression rates than neat HTPB in air counterflow, accompanied by frequent droplet ejections. High-speed digital inline holography enables observing particle ejections from the HTPB surface, revealing that the ejections are driven by the gas-bubble bursts from HTPB pyrolysis. *In-situ* heating in a TEM shows that the Cu coating facilitates cracking of the alumina oxide shell and the outflow of molten Al. Kinetic simulations and thermodynamic analysis show that the exposed Al reacts with back-diffused H_2O and CO_2, leading to sufficient heat generation that causes faster pyrolysis of HTPB into gaseous species and lifts the particles off the burning surface.

2. Methods

2.1. Synthesis, TG-DSC, and TOFMS

nAl@Cu were prepared via a one-pot synthetic route as detailed in Fig. S1(a) and Yang et al. [16], via an overall synthetic reaction presented in Equation (1). Briefly, nAl particles (100 nm, US Research Nanomaterials) were dispersed in a methanolic solution of 0.16 mol·L^{-1} $CuCl_2{\cdot}2H_2O$ (Acros Organics, 99%) under ultrasonication. A separate methanolic solution of 0.32 mol·L^{-1} NH_3BH_3 (Sigma-Aldrich, 90%) was then slowly added dropwise, and the mixture was sealed and maintained in a 313 K water bath with sonication for 80 mins. The resultant particles were washed with methanol, separated via centrifugation, and dried under vacuum. The obtained nAl@Cu particles are subsequently used as additives in HTPB formulations. TEM-EDS images of synthesized nAl@Cu showing Cu layers are in Fig. S1(b). Further inductively coupled plasma optical emission spectroscopy (ICP-OES) analysis after microwave-assisted acid digestion demonstrates that we had formed a Cu coating of ~12wt%. The powdered sample (5 mg) was weighed into a Teflon digestion vessel and digested using a MiniWAVE microwave digestion module (SCP Science, 6 × 75 mL configuration). Each sample was treated with nitric acid (HNO_3, 70%) and hydrochloric acid (HCl, 35%). Vessels were sealed and heated in the microwave with 100% power for 20 minutes with regulation point at 70 psi. After cooling, the digests were filtered and diluted with Millipore water for the following ICP-OES tests (PerkinElmer Optima 7300DV). Calibration standards were included to ensure analytical accuracy.

$$2CuCl_2 + NH_3BH_3 \rightarrow 2Cu + NH_4BCl_4 + H_2 \quad (1)$$

Composite fuel grains were made by mixing HTPB (RCS), prepolymerised diphenyl methane diisocyanate curative (MDI, RCS), and isodecyl pelargonate plasticizer (IDP, RCS) for 5 mins at 2000 rpm in a Thinky AR100 planetary mixer. Then 5–10wt% of nAl@Cu, nAl or micron-size Al (μAl, Valimet H-2) was added and mixed for another 10 mins at 2000 rpm. The resulting paste was then extruded into 1 mL syringes (ID ~4.8 mm) and stored in a fume hood for three days to fully cure. A table with a detailed breakdown of the fuel grain composition and their measured densities can be found in Table S1.

Thermogravimetric analysis (TGA) and differential scanning calorimetry (DSC) measurements were performed on a NETZSCH STA 449 F3 Jupiter. Approximately 3 mg of sample powder (either nascent nAl or nAl@Cu) was loaded into an alumina crucible and heated from room temperature to 1473 K at 1 K·min^{-1} under a continuous flow of high-purity Ar (50 mL min^{-1}). Airflow was used during TGA-DSC measurements on HTPB (and HTPB + nAl@Cu) samples. T-jump time-of-flight mass spectrometry (TOFMS) on HTPB with metal or metal oxide additives was performed at a heating rate of 3.5 × 10^5 K·s^{-1} under high vacuum (~10^{-6} Torr), following the same procedure described in detail elsewhere [16,17].

2.2. Color imaging and thermography

High-speed color imaging was performed at two different magnification levels to investigate macroscopic and microscopic combustion events, as described previously [28]. Macroscopic views used a Phantom Miro 110 camera with a Nikon AF Micro Nikkor lens (aperture set at f/16, spatial resolution ~25 μm·$pixel^{-1}$), while microscopic views employed a Phantom VEO710L camera coupled to a long working distance microscope lens (Infinity photo-optical model K2 DistaMax, CF-4 objective), which provides a spatial resolution of ~2.1 μm·$pixel^{-1}$, from a working distance of ~54 mm. An infrared camera (Telops, FAST M3K) was used to image and estimate the temperature of the pyrolyzing HTPB surface during combustion, as described previously [26].

Three-color imaging pyrometry was applied to the color-camera data to map surface temperatures as described elsewhere [30,31]. Briefly, the

raw intensities of the three-color channels (red, green, and blue; RGB) were extracted by debayering the Bayer pattern images. Temperatures were estimated at each pixel by taking ratios of the three-color channels (G/R, B/G, and B/R) and compared with theoretical temperatures assuming graybody emission. The cameras were calibrated with blackbody sources (ThorLabs SLS201L and Mikron M390) and have an expected uncertainty of ~200–300 K.

2.3. Digital inline holography (DIH)

Burning ejections were imaged by DIH after illuminating the burning fuel with a collimated, continuous-wave 532 nm laser (Coherent Verdi-V6), which was spatially filtered with a 5-μm pinhole and expanded to a 25 mm diameter beam by 10 and 100 mm plano-convex lenses (Thorlabs model P5W, C060TMD-A, and LA1509-A). The in-line holograms were recorded on a high-speed CMOS camera (Phantom Miro 110) at 4 kHz with 2 μs exposure time, using Nikon AF Micro Nikkor lens to achieve 20 μm·pixel^{-1} over a 2.5 × 2.5 cm field of view. A band-pass filter (Andover model 532FS02–50, 532 ± 1 nm) was mounted on the imaging optics to suppress combustion emissions, and the focal plane was positioned between the fuel rod and camera. A schematic of the DIH setup is displayed in Fig. S2(a), and its principle can be found in previous studies [27,32–35]. This DIH setup enabled high-contrast diffraction patterns of >20 μm particles to be captured for three-dimensional tracking and particle sizing, after numerical reconstruction based on the Fresnel approximation.

2.4. Stagnation-flow burner

Combustion evaluation of the composite grains was conducted using a stagnation flow burner, as shown in Fig. S2(b). The initial volumetric flow rate ($\dot{V}_0$) of air is controlled by a mass flow controller (MKS model 1179, and 247D 4-channel readout). This air is then flowed into a resistive heating tube (Omega 316 SS inline duct heater) with a thermocouple (type K) and a PID temperature controller (Inkbird) positioned right before the exit. A series of six stainless steel mesh disks (McMaster, 40 × 40 then 100 × 100 mesh disks, model 9317T552 and 9317T555) were placed at the 19-mm-diameter nozzle exit to collimate the airflow, as shown in Fig. S2(b). The density of the heated air (ρ_{air}) scales with temperature according to the ideal gas law in Equation (2). Thus, the final air velocity (u_{air}) is computed from $\dot{V}_0$ with gas density correction and normalized by the area of the nozzle (A_{nozzle}) in Equation (3).

$$\rho_{air} = \frac{PM_{air}}{RT_{air}} \tag{2}$$

$$u_{air} = \frac{\dot{V}_0}{A_{nozzle}}\left(\frac{T_{air}}{T_0}\right) \tag{3}$$

where T_{air} is the temperature of the air read by the thermocouple and T_0 is the initial temperature of the air (~298 K).

On the fuel side, we used a 4.8-mm-diameter and 1-cm-length cylindrical grain. To maintain a constant 10 mm gap between the fuel surface and the oxidizer nozzle, we implemented a laser–photoresistor feedback loop driving a stepper motor (Thorlabs DRV225 with BSC201 controller) via an Arduino Uno microcontroller board and custom C# script. Prior to ignition, the stepper motor retracts, and a fuel grain is loaded into the burner. The laser is positioned ~2 mm above the top of the burner and aligned with the photoresistor. The motor then extrudes until the laser line is interrupted by the fuel grain, setting the initial height. During combustion, the signal from the photoresistor is tracked, and the fuel grain is extruded once the signal threshold is reached. An example of the displacement and photoresistor signal can be seen in Fig. S12. After each run, the recorded time and position data are fit to a linear curve, where the slope, or the extrusion rate of the stepper motor, gives the regression rate of the fuel grain.

The strain rate, K (s^{-1}), quantifies the flux of gas to the surface of the fuel grain and is defined in Equation (4), where u_{air} is the velocity of the airflow, and d is the distance between the airflow nozzle and the fuel surface. In this work, d was set to 10 mm to allow for imaging with the different cameras.

$$K = \frac{u_{air}}{d} \tag{4}$$

2.5. In situ TEM-EDS

Reaction dynamics and composition characterization of nAl@Cu particles were probed in FEI Titan Themis 300 STEM with X-FEG electron gun at 200–300 kV under 10^{-7} Torr. nAl@Cu dispersions (sonicated in hexane) were drop-cast onto Protochips Fusion AX E-chips and mounted in the corresponding heating holder. HAADF imaging and EDS elemental mapping were performed simultaneously during a controlled temperature ramp from room temperature to 870 K, as detailed previously [16]. At each target temperature (like 870 K), the stage was held for 1 min to acquire EDS maps. The electron beam was blanked between acquisitions to minimize any beam-induced effects on the particles.

2.6. Kinetic and thermodynamic calculations

A one-dimensional counterflow diffusion flame model was implemented in Chemkin-Pro software using USC Mech II [36–39] to estimate the diffusion flux of N_2, O_2, H_2O, and CO_2 and temperature distributions (at K = 200 s^{-1} and T_{air} = 770 K). A multicomponent formulation is employed, and a boundary condition is used that specifies the mass flux rather than mass fraction, to allow back diffusion into the nozzle. Since the Chemkin model is for a pure-gas phase system, in order to model the solid fuel side, we assume that at the grain boundary, HTPB → C_4H_6 gas [4,40,41]. The inlet temperature of C_4H_6 is assumed to be that measured by the IR camera of the HTPB surface, while the temperature of the inlet air is set to that measured by a K-type thermocouple within the air nozzle. The velocity of C_4H_6 is calculated based on the fuel regression rate, while the velocity of air is designated according to the MFC. The temperature of the flame at various heights above the molten HTPB surface (x) was measured by the rapid insertion of a B-type thin-wire thermocouple (OMEGA P30R-008) coupled with radiation heat loss correction [42].

3. Results and discussion

3.1. TGA and DSC

Fig. 2(a-b) shows DSC curves of nAl and nAl@Cu heated in Ar at 1 K·min^{-1}. For uncoated nAl, no changes occur below the melting point of Al (~933 K). In contrast, nAl@Cu exhibits an early exothermic alloying reaction at approximately 640 K, forming Al_2Cu, followed by a distinct eutectic melting event around 821 K, as shown in the phase diagram in Fig. S3 [16,19]. Although the alloying reaction is modestly exothermic (ΔH ≈ –40 J per gram sample), the formation of Al_2Cu significantly lowers the melting temperature of Al by approximately 100 K. These results underpin our hypothesis and motivation for using copper: The Cu layer induces early eutectic melting and potentially earlier alumina shell cracking at lower temperatures [16]. This phenomenon is expected to expose fresh aluminum surfaces earlier in the combustion process, enhancing reactivity and enabling rapid oxidation [16]. Consequently, we anticipate that the copper coating facilitates energetic particle ejections from the polymer surface, reducing agglomeration and improving combustion stability.

Fig. 2(c) compares the TGA curves of cured HTPB (black) and cured HTPB+5% nAl@Cu (red) in air, showing that the initial mass loss of HTPB starts ~40 K earlier with the addition of nAl@Cu, and the whole

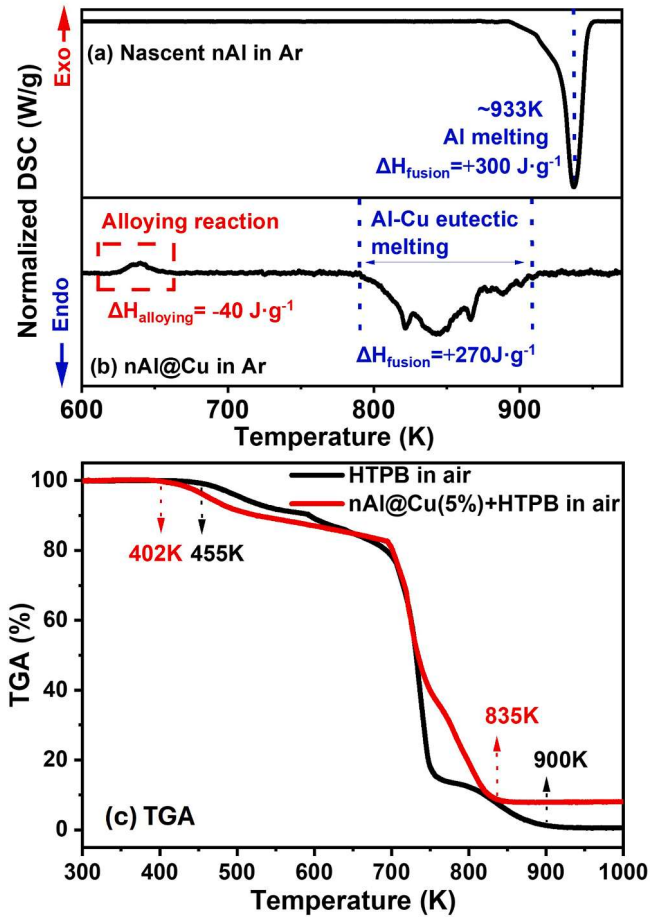

Fig. 2. DSC of (a) nAl and (b) nAl@Cu in argon at a heating rate of 1 K·min^{-1} and (c) TGA of HTPB (black) and HTPB+5% nAl@Cu (red) in air.

process completes 65 K earlier. However, in argon, no enhancement was observed, as shown in Fig. S4. There are two possible reasons for the earlier decomposition of HTPB with nAl@Cu in air: (1) the formation of metal oxides in air, since it is known that the addition of CuO can support HTPB decomposition [43]. As shown in Fig. S5, T-jump TOFMS of HTPB in vacuum (10^{-6} Torr, heating rate 3.5×10^5 K·s^{-1}) shows that the onset temperature of 1,3-butadiene release ($m/z = 54$, major product of HTPB decomposition) is ~60 K lower with the addition of CuO nanoparticles. (2) Earlier alumina shell cracking of nAl@Cu allows the exposed Al core to react with air components, releasing heat to accelerate HTPB decomposition.

3.2. *High-speed imaging and thermography*

Combustion of fuel grains made of HTPB, nAl/HTPB (5/95wt%), and nAl@Cu/HTPB (5/95wt%) were studied with an air stagnation flow burner (Fig. S2), and the flame structures were recorded with high-speed imaging as in Fig. 3. At strain rates of 100–300 s^{-1}, the burning HTPB fuel surface develops a convex, hemispherical shape as it regresses, with the flame front wrapping around the HTPB dome (Fig. 1(a)). This flame structure was observed for both HTPB and nAl@Cu/HTPB, whose combustion remained stable. However, the nAl/HTPB fuel typically fails to sustain a flame within 2 mm of regression due to nAl aggregation on the surface (Fig. 3(b)), gradually forming an alumina crust layer that retards further propagation (bright parts in white box).

In contrast, nAl@Cu/HTPB (5–10wt%) burned steadily, with no aggregation on the surface throughout the whole combustion (~1-cm-long fuel), exhibiting frequent ejection of small burning droplets from the surface and dispersing into the flame, as shown with a representative ejection event spanning 8 ms in the time-resolved snapshots in Fig. 3(a). At strain rates < 100 s^{-1}, the flame tip sat several mm above the surface. At strain rates > 100 s^{-1}, the flame shape becomes a dome, closely following the shape of the HTPB surface. This flame transition is shown in Fig. S6. According to the kinetic simulation in Fig. S7 (method detailed in section 2.6), the flame sits ~1 mm above the stagnation point, which is common for sooty flames [23].

Infrared thermography captured the fuel-surface temperature through the semi-transparent flame seen in Fig. 3(d). The surface temperature lies in the range of 700–840 K, consistent with reported HTPB pyrolysis temperatures and our TG results [4,41,44,45], indicating a pyrolysis-limited steady-state. Notably, the presence of nAl@Cu in the HTPB did not significantly alter the average surface temperature, probably because energy released by nAl@Cu surface reactions is absorbed by the surrounding HTPB to increase its decomposition. IR frames also revealed transient "cold spots" (~700–750 K), which correlate with gas bubbles (mainly 1,3-butadiene and 4-vinyl cyclohexane [4]) formed from the endothermic depolymerization in the molten HTPB layer (near ~720 K, $\Delta H_{\text{HTPB-depolymerization}} \sim +0.1$ kJ g^{-1}) [40,41].

Three-color pyrometry of the nAl@Cu/HTPB in Fig. 3(c) shows that ejected particles burned at ~2500–3500 K as they mix with the oxidizer stream. Such intense, sustained incandescent specks were essentially absent in neat HTPB and nAl/HTPB. The plentiful hot droplets in the nAl@Cu case confirm that these copper-coated additives are ignited and release energy via intense combustion immediately upon detachment from the surface. Together, these diagnostics demonstrate that nAl@Cu uniquely drives high-temperature secondary combustion via particle ejection, while the primary flame shape and mean surface temperature remain governed by HTPB pyrolysis and flow conditions. Uncoated nAl, by contrast, coalesces on the fuel surface and eventually extinguishes the flame. Thus, efficient particle detachment and efficient combustion are essential for sustaining stable combustion in aluminized solid fuels.

3.3. *Particle ejection dynamics via DIH*

While standard high-speed imaging captures particles after they ignite above the flame front, it does not resolve how and why they lift off in the first place when uncoated nAl does not. To see the very start of ejection, we employed high-speed DIH, which records the entire journey of particles from the fuel surface into the airflow (Fig. 4). As shown in Fig. 4(a), the HTPB molten layer sporadically forms gas bubbles that grow within milliseconds and subsequently burst (at ~1–1.75 ms), but no droplets were seen to be expelled. In contrast, each bubble burst in the nAl@Cu/HTPB composite launches numerous particles being violently ejected from the surface (Fig. 4(b)). These ejected particles are propelled away from the grain into the flame front, where they then ignite and glow incandescent (as captured in Fig. 4). It should be noted that such ejections were not seen in nAl/HTPB, as shown in Fig. 4(e). The direct comparison of Fig. 4(a-b) indicates that the driving force for particle ejections is likely the expansion of gaseous products from HTPB decomposition bursting through the molten fuel. Because such energetic bubble-burst ejection events with high frequency are only observed in the nAl@Cu/HTPB fuel, the chemical reactivity of nAl@Cu compared to nAl is further examined with *in situ* TEM and calculations in Section 3.5.

In addition to qualitative insights, DIH provides quantitative measures of particle sizes and speeds. For nAl@Cu/HTPB, the DIH setup (20 μm·pixel^{-1}) size distribution is shown in Fig. 4(c), yielding a log-normal fitted average detected particle diameter of ~85 μm; however, higher-magnification DIH (Fig. S8, 1.4 μm·pixel^{-1}) reveals that many fragments are much smaller than the 20-μm detection limit, so the plotted distribution should be taken as an upper bound. As shown in Fig. 4(d), the distribution of ejection speeds typically ranges from 1 to 6 m·s^{-1} with an average of 3.0 m·s^{-1}. This leads to a calculated average stopping distance of ≥1 cm in static air at 770 K, implying that the particles of micron sizes could cross the stagnation point and enter the flame. In

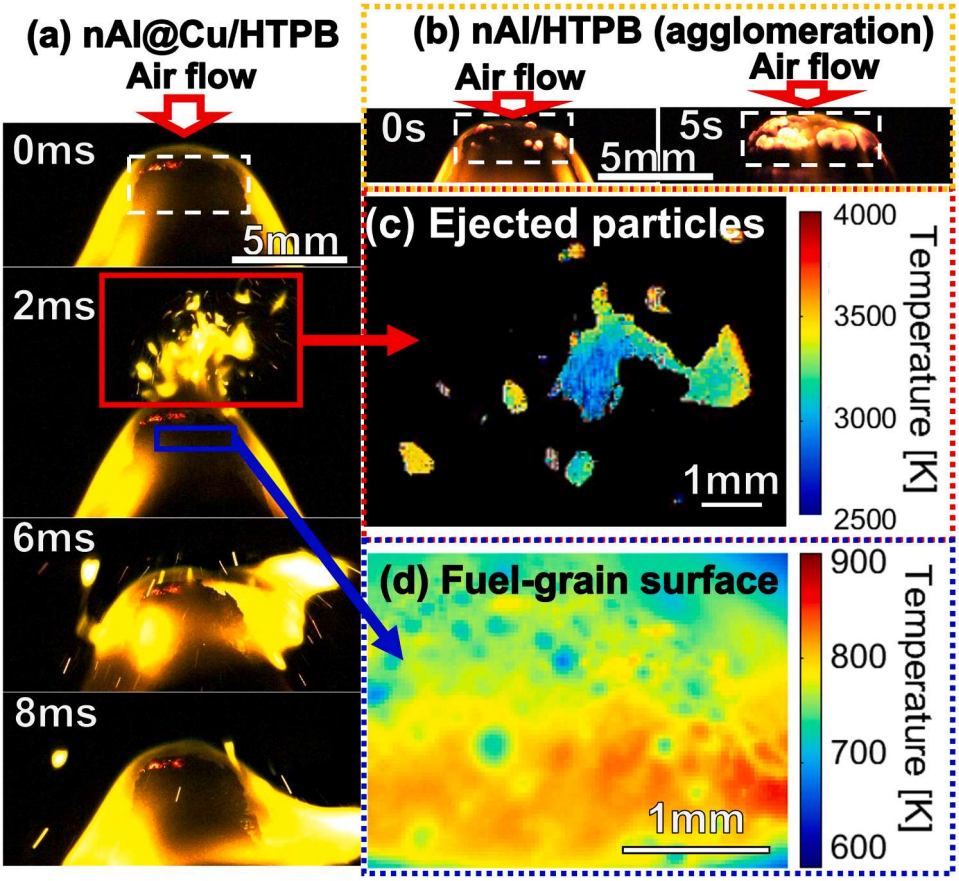

Fig. 3. Snapshots of air-breathing counterflow of (a) nAl@Cu/HTPB (5/95 wt%) and (b) agglomeration of nAl/HTPB; (c) three-color imaging pyrometry of ejected particles of nAl@Cu/HTPB (Video S1-S3); (d) IR thermography of the fuel-grain surface.

contrast, sub-microparticles or nanoparticles with much smaller stopping distances probably do not make it to the flame. Taken together, these DIH results show that the Cu shell enables gas-driven ejection of nAl, effectively clearing them from the burning surface, in contrast to uncoated nAl/HTPB where ejections are rare. This efficient release of particles is thus an essential factor in preventing Al agglomeration and sustaining stable combustion.

3.4. Regression rates

At an air temperature of 770 K in counterflow, HTPB fuel exhibited a baseline regression rate that increased markedly with the imposed strain rate (Fig. 5). Specifically, the regression rate of the pure HTPB sample rose from around 0.16 mm·s^{-1} at a low strain rate (100 s^{-1}) to approximately 0.32 mm·s^{-1} at the highest strain (300 s^{-1}), agreeing with previous studies at similar temperature [46]. To evaluate the impact of aluminum additives, since nAl/HTPB fails to continuously propagate (regression rate = 0), 5 wt% μAl was incorporated into HTPB. At a strain rate of 100 s^{-1}, the μAl/HTPB burned slower (0.11 mm·s^{-1}) than HTPB (0.16 mm·s^{-1}), indicating that the presence of coarse Al particles initially suppressed the regression rate. At the highest strain tested (300 s^{-1}), the μAl/HTPB sample achieved only around 0.26 mm·s^{-1}, well below that of the neat HTPB. Thus, the addition of 5% μAl tends to reduce the regression rates compared to neat HTPB, consistent with previous studies [14]. One of the main limitations of micron-Al in propellants is its low-combustion efficiency, mainly caused by incomplete oxidation [47]. Ignition temperature of micron-Al is>1000 K higher than the surface temperature of HTPB (700–840 K, Fig. 3(d)) [1, 2]. Therefore, they cannot be ignited within the Al/HTPB matrix, although they may get partially ignited and oxidized after being ejected above the stagnation point.

In contrast, replacing μAl with an equal loading (5 wt%) of nAl@Cu yielded a distinctly improved trend. Even at low strain, the nAl@Cu/HTPB (5/95%) composite outperformed both HTPB and μAl/HTPB, and the performance advantage widened with increasing strain rate. These results demonstrate that a small addition of nAl@Cu can enhance or at least maintain the regression rate relative to neat HTPB, in stark contrast to the suppression observed with μAl or nAl. A similar effect was also evident at the lower airflow temperature of 470 K (Fig. S9). Increasing the nAl@Cu content to 10wt% led to further improvement, achieving the highest regression rates across all conditions (0.40 mm·s^{-1}). At elevated strain, the 10wt% formulation significantly outpaced both HTPB and μAl/HTPB, underscoring the effectiveness of higher nAl@Cu loading in promoting faster burning. Power-law fits to these trends are summarized in Table S2.

It is known that the addition of metal oxides, specifically CuO, can enhance the regression rate of HTPB [43]. As a result, nano-Cu powder (nCu) was added to HTPB to probe whether Cu is catalyzing the decomposition of HTPB. The Al@Cu/HTPB composites contain ~1.2 wt % Cu in the composite. It was found that the addition of 1–2 wt% nCu powder did not significantly affect the regression rate of HTPB (Fig. S10). Therefore, the enhanced regression rate of HTPB is probably attributed to the early alumina shell cracking of nAl@Cu that allows the exposed Al core the react with air composites, releasing heat to accelerate HTPB decomposition.

Overall, these results clearly illustrate the distinct influences of micron versus nano-sized Al additives on HTPB combustion. μAl particles showed limited reactivity and led to reduced regression rates. In contrast, the reactive copper-coated nAl significantly boosted combustion rates, particularly at higher loading (10 wt%). This enhancement

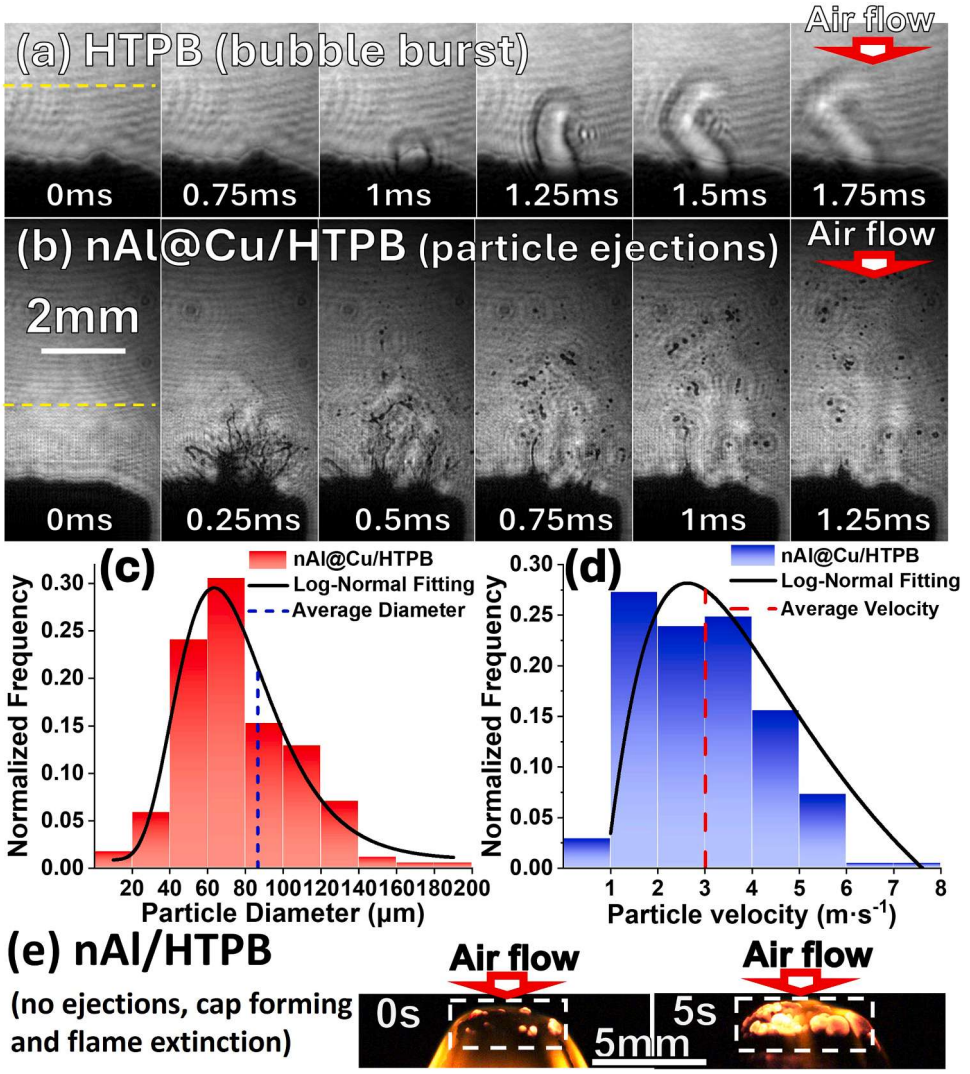

Fig. 4. Reconstructed holograms of (a) burst bubble in HTPB and (b) particle ejections in nAl@Cu/HTPB (5/95 wt%), where the yellow lines present the position of flame fronts (Video S4). (c) Particle sizes (upper limits) and (d) initial velocity distributions in nAl@Cu/HTPB are shown with their log-normal fittings. (e) nAl/HTPB has no ejections (Al_2O_3-cap formation viewed by color imaging).

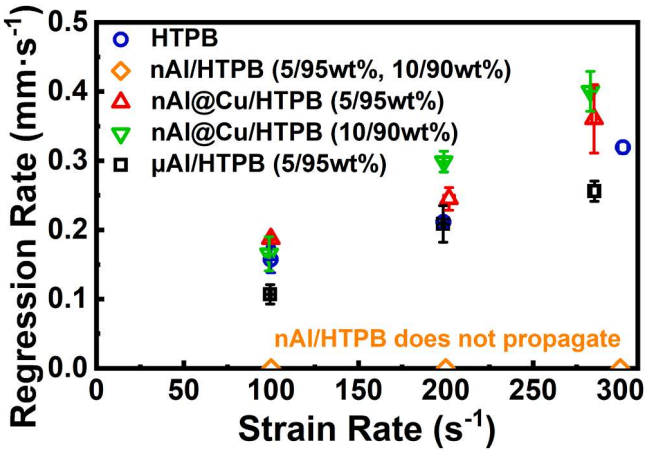

Fig. 5. Regression rates of the various fuel grains at T_{air}=770 K, including HTPB, μAl/HTPB (5/95 wt%), and nAl@Cu/HTPB (5/95 wt% and 10/90 wt%).

likely arises from the Cu coating facilitating Al ignition at lower temperatures via eutectic melting, thereby actively contributing heat and gas generation to accelerate HTPB pyrolysis and sustain combustion without particle agglomeration.

3.5. Mechanism

In air-breathing solid-fuel systems, gases from pyrolysis presumably lift particles, making nanoparticle ejection critically dependent on pyrolysis-driven gas dynamics. Zhou et al. [10] elucidated this phenomenon through molecular dynamics simulations, showing that the polymer–particle interfacial forces between nAl and HTPB exceed the kinetic energy imparted to nanoparticles by the blowing force from HTPB decomposition. Since pyrolysis-generated gas forces alone cannot overcome the adhesive and surface-tension forces binding nanoparticles to the molten polymer, additional energy input is required to provide sufficient thrust for particle ejection. Our experimental results align closely with this reasoning: uncoated nAl particles in HTPB failed to detach at typical HTPB surface temperatures (~700–840 K), instead forming a crust alumina layer (Fig. 3(b)) that ultimately extinguished combustion.

To clarify why the nAl@Cu outperformed uncoated nAl, we conducted *in situ* TEM heating experiments on individual nanoparticles. When heated in vacuum (~10^{-7} Torr), bare Al nanoparticles exhibited

no signs of molten aluminum release until temperatures surpassed aluminum's melting point (~933 K), as shown in Fig. 6(a). The robust alumina shell (5–10 nm thick) encapsulated the molten Al, preventing effective interaction with the surroundings. Thus, for nAl embedded in HTPB, the <900 K surface temperature alone is insufficient for shell rupture, leaving these particles inert, undergoing slow oxidation, and prone to accumulation at the surface.

In contrast, *in situ* TEM heating of nAl@Cu particles showed the appearance of nano-cracks and molten Al extrusions through the oxide shell starting at 670–830 K (Fig. S11 and Fig. 6(b)), close to the HTPB surface temperature range measured by the IR imaging (Fig. 3(d), 700–840 K) and previous studies [46]. Al–Cu alloying reactions enable the formation of Al_2Cu alloy, which significantly lowers the eutectic melting point (~821 K) as was seen in TG-DSC in Fig. 2(a) [19]. This clearly indicates that the Cu coating promotes early melting and oxide-shell rupture, exposing fresh molten Al surfaces at lower temperatures. The breached shell allows the nanoparticle to engage directly in oxidation reactions, initiating exothermic events that promote the surrounding HTPB to pyrolyze and generate gas thrusts.

To summarize thus far, the Cu coating lowers the melting point of Al via eutectic formation and promotes shell cracking, which enables the core aluminum to become chemically accessible. However, early melting and exposure alone do not guarantee particle ejection. For Al to lift off the surface, it must release sufficient energy to rapidly decompose the surrounding HTPB and generate enough gas-phase products to entrain the particle into the oxidizer flow. Since the flame zone is diffusion-limited and depleted in molecular O_2 near the fuel surface, the identity of the oxidizing species becomes critical. Therefore, we conducted kinetic flame simulations ($K = 200\ s^{-1}$ and $T_{air} = 770$ K) to determine what gaseous species actually reach the surface and

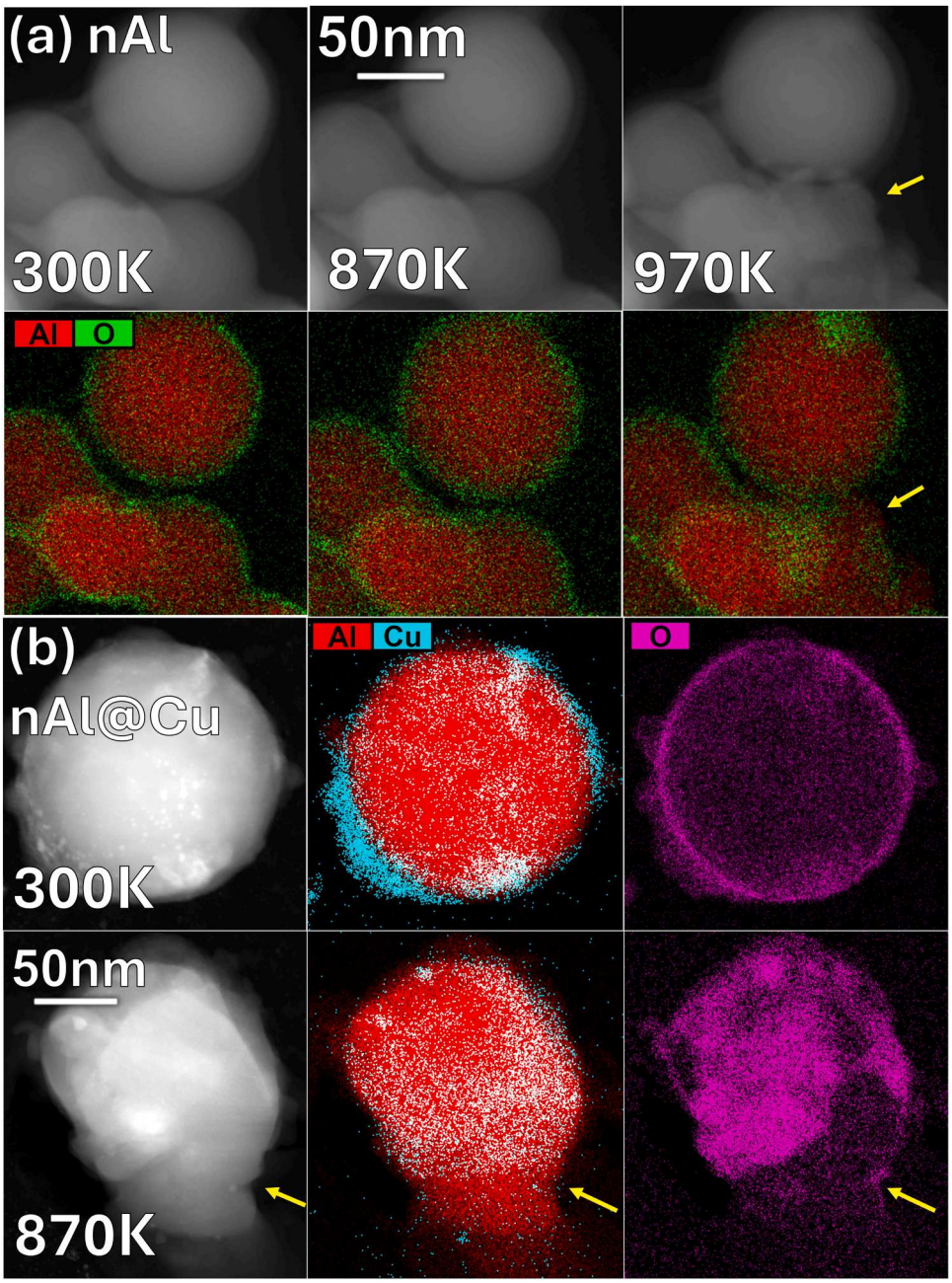

Fig. 6. *In situ* TEM and EDS of heated (a) nascent nAl and (b) nAl@Cu, showing nano-cracks in the alumina shell and leakage of the molten Al core after being heated above the Al-Cu eutectic melting point.

participate in Al oxidation, and whether the associated heat release is sufficient to drive particle ejection.

Fig. 7 shows the simulated distributions of the gas-phase species of interest (H_2O, CO_2, N_2, and O_2) and the flame temperature. The measured and simulated flame temperature profiles align well and support the reliability of the simulation. Both H_2O and CO_2 can diffuse to the surface of HTPB and may act as the oxidizer for Al particles here. In contrast, the concentration of O_2 is too low to oxidize Al. The reaction of N_2 with Al was also ruled out with additional experiments, by using Ar to replace N_2 in air, which led to similar regression rates, as shown in Fig. S13.

Diffusion fluxes of H_2O and CO_2 (J_{H_2O} and J_{CO_2}) near the fuel surface (0–0.1 cm) were estimated using Equation (5).

$$J_i = -D_i\frac{dc_i}{dx} \tag{5}$$

where J_i is the diffusion flux, D_i is the diffusion coefficient (obtained from USC Mech II), and dc/dx is the concentration gradient. Calculations yielded fluxes of $J_{H_2O} = 0.085\ \text{mol}\cdot\text{m}^{-2}\cdot\text{s}^{-1}$ and $J_{CO_2} = 0.03\ \text{mol}\cdot\text{m}^{-2}\cdot\text{s}^{-1}$. To estimate Al consumption, the molar flux of Al (J_{Al}) from the regressing fuel surface was computed using Equation (6).

$$J_{Al} = \frac{v\cdot\rho_{HTPB}\cdot w_{Al}}{M_{Al}} = 0.3\ \text{mol}\cdot\text{m}^{-2}\cdot\text{s}^{-1} \tag{6}$$

where v is the measured regression rate, ρ_{HTPB} is the density of HTPB, w_{Al} is the weight percentage of Al, M_{Al} is the molar mass of Al. The calculated diffusion fluxes of H_2O and CO_2 allow partial oxidation of Al, and the total heat release from its reaction with H_2O and CO_2 ($\Delta H_{oxidation}$) can be calculated with Eqs. (7)-(9).

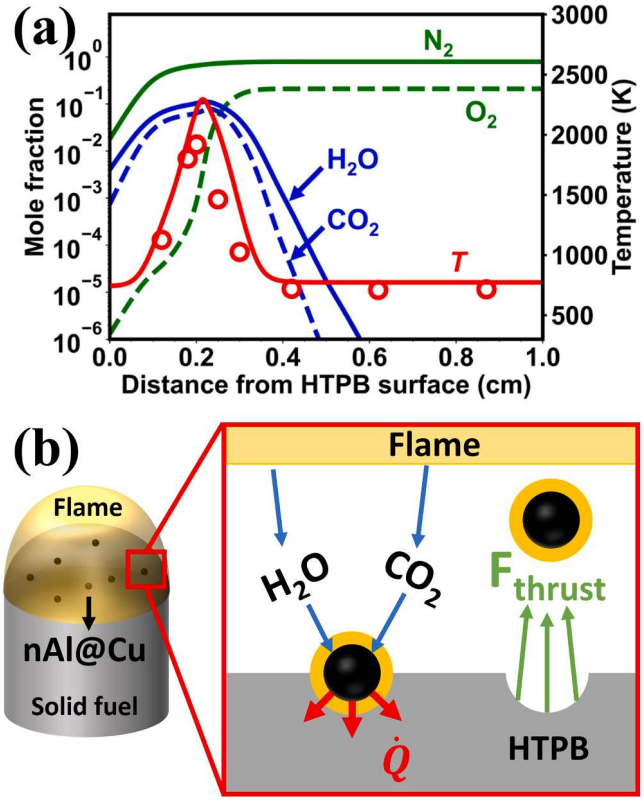

Fig. 7. (a) Simulated profiles of gas-phase temperature (red line), mole fraction of H_2O (blue solid line), CO_2 (blue dashed line), N_2 (green solid line), and O_2 (green dashed line). Thermocouple-measured flame temperatures are shown in red circles. (b) Schematic of the ejection of nAl@Cu from the HTPB surface.

$$\text{Al} + 1.5H_2O = 0.5Al_2O_3 + 1.5H_2,\quad \Delta H_1 = -487\,\text{kJ}\cdot\text{mol}^{-1} \tag{7}$$

$$\text{Al} + 0.75CO_2 = 0.5Al_2O_3 + 0.75C,\quad \Delta H_2 = -553\,\text{kJ}\cdot\text{mol}^{-1} \tag{8}$$

$$\Delta H_{oxidation} = a_{H_2O}\cdot\Delta H_1 + a_{CO_2}\cdot\Delta H_2 = -166\,\text{kJ}\cdot\text{mol}^{-1} \tag{9}$$

where $a_{H_2O} = 0.189$ and $a_{CO_2} = 0.133$ represent the molar fractions of Al oxidized by H_2O and CO_2 based on their diffusion fluxes. Previous studies [40,41] indicate the primary mass-loss step in HTPB pyrolysis near ~720 K is endothermic ($E_{HTPB} = \Delta H_{HTPB\text{-}depolymerization} \sim +0.1\ \text{kJ}\cdot\text{g}^{-1}$). Assuming that the energy released from the partial oxidation of an aluminum-nanoparticle volume (V_{Al}) transfers directly to pyrolyze surrounding HTPB, the volume ratio of pyrolyzed HTPB (V_{HTPB}) to Al consumed can be calculated by Equation (10).

$$\frac{V_{HTPB}}{V_{Al}} = \frac{-\Delta H_{oxidation}\cdot\rho_{Al}}{M_{Al}\cdot E_{HTPB}\cdot\rho_{HTPB}} \sim 10^2 \tag{10}$$

This estimation demonstrates that even partial oxidation of Al releases enough heat to rapidly pyrolyze substantial surrounding HTPB [48]. Consequently, as shown in Fig. 7(b), the rapid local pyrolysis significantly reduces particle-polymer adhesion, generating vigorous gas expansion capable of ejecting nAl@Cu from the fuel surface, effectively preventing surface agglomeration and sustaining stable combustion.

In summary, the burn rate of nAl@Cu/HTPB increases due to increased surface reactions, as shown in Fig. 8 and explained below: The 700–840 K surface temperature in Fig. 3(d) is mainly controlled by the decomposition temperature of HTPB in Fig. 2(c). According to *in-situ* TEM in Fig. 6(b) and TG-DSC in Fig. 2(b), nAl@Cu would have shell cracking at a similar temperature range, leading to Al outward flow to react with CO_2 and H_2O, based on the kinetic simulations in Fig. 7(a). The heat released by the surface reactions of nAl@Cu + CO_2/H_2O is absorbed by the surrounding HTPB matrix to increase its decomposition to gas-phase products, leading to both faster regression rates and particle ejections.

4. Conclusion

This study overcomes one of the limitations in using nanoparticles in a polymer fuel. Namely, the high interfacial binding energy retards particle lift-off from the surface of the fuel, leading to agglomeration and surface quenching. Here, we demonstrate a strategy of driving low-temperature Al-Cu alloying and low eutectic melting using a core-shell nAl@Cu to enable sustained, air-breathing combustion of HTPB. This overcomes the agglomeration and flame quenching that plagues uncoated nAl additives. The low-temperature alloying, along with back diffusion of H_2O and CO_2 diffusion results in surface oxidation and sufficient heat release to pyrolyze a volume of HTPB approximately one hundred times the nAl@Cu particle's volume, generating sufficient gaseous products to propel the particle off the surface and sustain combustion. *In situ* TEM confirms shell rupture and molten Al extrusion. As a result, nAl@Cu/HTPB composites can achieve higher regression rates compared to uncoated Al composites. These findings establish nAl@Cu as a powerful additive for air-breathing fuels, offering a pathway toward lighter, higher-energy-density propulsion systems without traditional solid oxidizers.

CRediT authorship contribution statement

Lei Yang: Writing – original draft, Investigation, Formal analysis, Data curation. **Erik Hagen:** Writing – original draft, Investigation, Formal analysis, Data curation. **Yuxin Zhou:** Writing – review & editing, Data curation. **Keren Shi:** Writing – review & editing, Data curation.

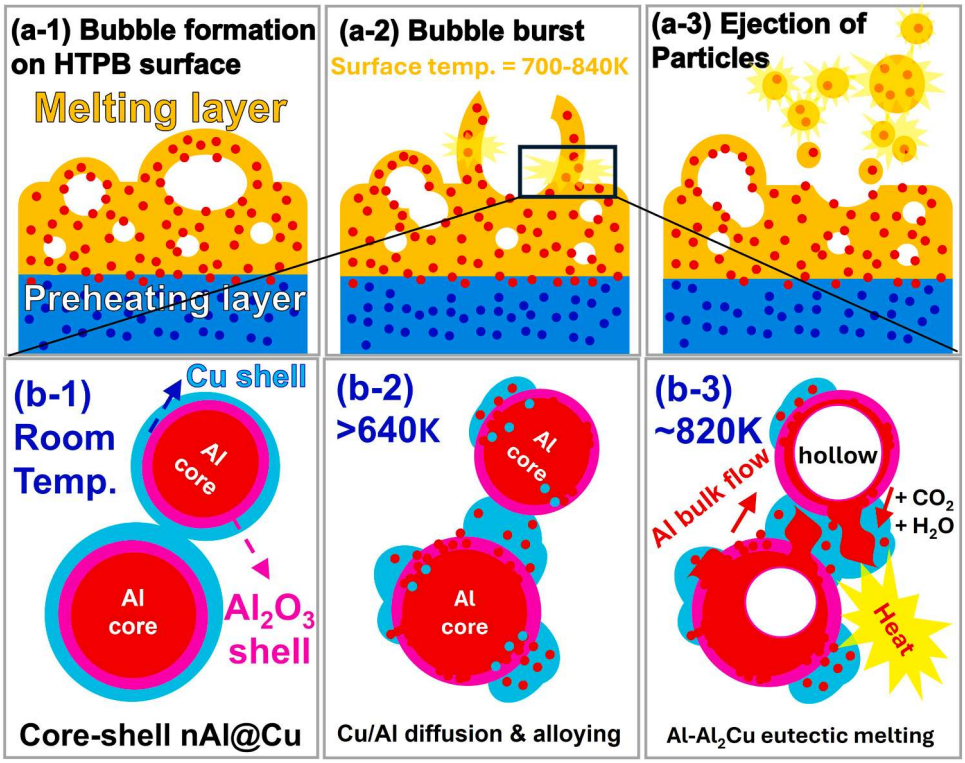

Fig. 8. Illustration of the particle-ejection and faster-combustion mechanism of nAl@Cu/HTPB.

Yuan Qin: Writing – review & editing, Data curation. **Michael R. Zachariah:** Writing – review & editing, Supervision, Resources, Project administration, Methodology, Investigation, Funding acquisition, Conceptualization.

Declaration of competing interest

On behalf of all the authors, we declare no conflict of interest. This work is original and has not been considered for publication elsewhere.

Acknowledgments

This work was supported by the ONR.

Supplementary materials

Supplementary material associated with this article can be found, in the online version, at doi:10.1016/j.combustflame.2026.114799.

References

[1] E.L. Dreizin, Metal-based reactive nanomaterials, Prog. Energy Combust. Sci 35 (2009) 141–167.
[2] D. Sundaram, V. Yang, R.A. Yetter, Metal-based nanoenergetic materials: synthesis, properties, and applications, Prog. Energy Combust. Sci 61 (2017) 293–365.
[3] C. Dennis, B. Bojko, On the combustion of heterogeneous AP/HTPB composite propellants: a review, Fuel 254 (2019) 115646.
[4] Y. Qian, Z. Wang, L. Chen, P. Liu, L. Jia, B. Dong, H. Li, S. Xu, A study on the decomposition pathways of HTPB and HTPE pyrolysis by mass spectrometric analysis, J. Anal. Appl. Pyrolysis 170 (2023) 105929.
[5] Y.K. Sinha, B.T.N. Sridhar, R. Kishnakumar, Study of thermo-mechanical properties of HTPB–paraffin solid fuel, Arab, J. Sci. Eng 41 (2016) 4683–4690.
[6] K. Shi, Y. Wang, G.I. Paul, M.R. Zachariah, The influence of heat feedback and thermal conductivity on the burn rate of thermite composites, Combust. Flame 269 (2024) 113593.
[7] F. Maggi, S. Colciago, C. Paravan, S. Dossi, L. Galfetti, Exploratory investigations on metal-based fuels for air-breathing propulsion, Prog. Propul. Phys 11 (2019) 699–712.
[8] A.M. Robinson, D. Ka, X. Zheng, Y. Xia, Perfluoroalkyl-functionalized HTPB improves the mechanical and combustion performance of boron/HTPB composites as solid fuel, ACS Appl. Polym. Mater 6 (2024) 12654–12660.
[9] Y. Jiang, J. Leem, A.M. Robinson, S. Wu, A.H. Huynh, D. Ka, R.R. Zhao, Y. Xia, X. Zheng, Tailoring the mechanical and combustion performance of B/HTPB composite solid fuel with covalent interfaces, Compos. Sci. Technol 245 (2024) 110350.
[10] Y. Zhou, M.R. Zachariah, Computational study on the lifting of aluminum particles from a hydroxyl-terminated polybutadiene burning surface, J. Phys. Chem. C 129 (2025) 5696–5701.
[11] G. Young, G. Risha, A.G. Miller, R.A. Glass, J. Terrence L. Connell, R.A. Yetter, Combustion of alane-based solid fuels, Int. J. Energ. Mater. Chem. Propuls 9 (2010) 249–266.
[12] J. Yuan, J. Liu, Y. Zhou, J. Wang, T. Xv, Aluminum agglomeration of AP/HTPB composite propellant, Acta Astronaut 156 (2019) 14–22.
[13] S. Li, X. Lv, L. Liu, S. Yue, P. Liu, W. Ao, Comparative study on aluminum agglomeration characteristics in HTPB and NEPE propellants: the critical effect of accumulation, Combust. Flame 249 (2023) 112607.
[14] G. Young, G.A. Risha, T.L. Connell Jr., R.A. Yetter, Combustion of HTPB based solid fuels containing metals and metal hydrides with nitrous oxide, Propellants Explos. Pyrotech 44 (2019) 744–750.
[15] F. Noor, A. Vorozhtsov, M. Lerner, E.P. Bandarra Filho, D. Wen, Thermal-chemical characteristics of Al–Cu alloy nanoparticles, J. Phys. Chem. C 119 (2015) 14001–14009.
[16] L. Yang, Y. Zhou, M. Chowdhury, Y. Qin, M.M. Dickson, M.R. Zachariah, Synergistic transition multi-metal coatings drive sub-melting-point reaction of aluminum, Chem. Eng. J 519 (2025) 164794.
[17] Y. Zhou, L. Yang, A.K. Vasudevan, M. Dickson, M. Chowdhury, K. Shi, M. R. Zachariah, Nickel-coated aluminum nanoparticles for modulating ignition temperature: interfacial chemistry and mechanism, ACS Appl. Eng. Mater 3 (2025) 2346–2353.
[18] J. Zhang, F. Zhao, H. Li, Z. Yuan, M. Zhang, Y. Yang, Q. Pei, Y. Wang, X. Chen, Z. Qin, Improving Ignition and Combustion Performance of Al@Ni in CMDB Propellants: effect of Nickel Coating, Chem. Eng. J 456 (2023) 141010.
[19] C. Zhou, L. Jiang, Z. Gu, C. Wang, L. He, L. Huang, Z. Li, K. Li, Flexible core-shell structured Al-Cu alloy phase change materials for heat management, Chem. Eng. J 471 (2023) 144610.
[20] C.M. Geipel, B.T. Bojko, C.J. Pfützner, B.T. Fisher, R.F. Johnson, Regression of solid polymer fuel strands in opposed-flow combustion with gaseous oxidizer, Proc. Combust. Inst 39 (2023) 3389–3399.
[21] X. Hui, D. Zheng, W. Tan, X. Xue, W. Liu, The effects of hydrogen addition on soot formation in counterflow diffusion *n*-heptane flames, Int. J. Hydrog. Energy 48 (2023) 8707–8715.
[22] J. Yu, H. Meng, A numerical study of counterflow diffusion flames of methane/air at various pressures, Sci. China Technol. Sci 57 (2014) 615–624.

[23] Y. Wang, S.H. Chung, Soot formation in laminar counterflow flames, Prog. Energy Combust. Sci 74 (2019) 152–238.
[24] G. Young, S. Hromisin, S. Loeffler, T.L.C. Jr, Effect of oxidizer type on solid fuel combustion, J. Propuls. Power 36 (2019) 2.
[25] K. Shi, M. Bokhoor, Y. Wang, T.P. Weihs, M.R. Zachariah, Propagation rate and product modulation in SHS reactions via focused microwave heating, Chem. Eng. Sci 302 (2025) 120794.
[26] K. Shi, Y. Wang, M.R. Zachariah, Microwave antenna focusing for spatially resolved modulation of burn rate, Chem. Eng. J 492 (2024) 152192.
[27] Y. Chen, D.R. Guildenbecher, K.N.G. Hoffmeister, M.A. Cooper, H.L. Stauffacher, M.S. Oliver, E.B. Washburn, Study of aluminum particle combustion in solid propellant plumes using digital in-line holography and imaging pyrometry, Combust. Flame 182 (2017) 225–237.
[28] Y. Wang, E. Hagen, P. Biswas, H. Wang, M.R. Zachariah, Imaging the combustion characteristics of Al, B, and Ti composites, Combust. Flame 252 (2023) 112747.
[29] H. Wang, E. Hagen, K. Shi, S. Herrera, F. Xu, M.R. Zachariah, Carbon fibers as additives to engineer agglomeration and propagation of aluminized propellants, Chem. Eng. J 460 (2023) 141653.
[30] D.J. Kline, Z. Alibay, M.C. Rehwoldt, A. Idrogo-Lam, S.G. Hamilton, P. Biswas, F. Xu, M.R. Zachariah, Experimental observation of the heat transfer mechanisms that drive propagation in additively manufactured energetic materials, Combust. Flame 215 (2020) 417–424.
[31] D.J. Kline, M.C. Rehwoldt, J.B. DeLisio, S.C. Barron, H. Wang, Z. Alibay, J. C. Rodriguez, G.M. Fritz, M.R. Zachariah, In-operando thermophysical properties and kinetics measurements of Al-Zr-C composites, Combust. Flame 228 (2021) 250–258.
[32] J. Huang, S. Li, W. Cai, Y. Qian, E. Berrocal, M. Aldén, Z. Li, Quantification of the size, 3D location and velocity of burning iron particles in premixed methane flames using high-speed digital in-line holography, Combust. Flame 230 (2021) 111430.
[33] Y.C. Mazumdar, M.E. Smyser, J.D. Heyborne, M.N. Slipchenko, D. R. Guildenbecher, Megahertz-rate shock-wave distortion cancellation via phase conjugate digital in-line holography, Nat. Commun 11 (2020) 1129.
[34] L. Yang, K. Shi, Y. Zhou, M. Chowdhury, A. Anis, M.R. Zachariah, Thermal and holography imaging of heat feedback enables strategies to drive sustained combustion in highly reactive thermite composites, Chem. Eng. J 527 (2026) 171223.
[35] L. Yang, Y. Qin, L. Gabriel, E. Hagen, M. Zachariah, Interface Reaction in Core-Shell Boron-FeF_3: direct Observation of Gas Release and Oxide Removal during Combustion, ACS Appl. Mater. Interfaces 18 (2026) 3772–3780.
[36] S.G. Davis, A.V. Joshi, H. Wang, F. Egolfopoulos, An optimized kinetic model of H_2/CO combustion, Proc. Combust. Inst 30 (2005) 1283–1292.
[37] A.D. Abid, J. Camacho, D.A. Sheen, H. Wang, Quantitative measurement of soot particle size distribution in premixed flames – the burner-stabilized stagnation flame approach, Combust. Flame 156 (2009) 1862–1870.
[38] Hai Wang, Xiaoqing You, Ameya V. Joshi, Scott G. Davis, Alexander Laskin, Fokion Egolfopoulos & Chung K. Law, USC Mech Version II. High-Temperature Combustion Reaction Model of H_2/CO/C1-C4 Compounds. http://ignis.usc.edu/USC_Mech_II.htm, May 2007.
[39] ANSYS Chemkin Theory Manual 17.0 (15151), Reaction Design, San Diego, 2015.
[40] D. Tingfa, Thermal decomposition studies of solid propellant binder HTPB, Thermochim. Acta 138 (1989) 189–197.
[41] J.K. Chen, T.B. Brill, Chemistry and kinetics of hydroxyl-terminated polybutadiene (HTPB) and diisocyanate-HTPB polymers during slow decomposition and combustion-like conditions, Combust. Flame 87 (1991) 217–232.
[42] J. Camacho, C. Liu, C. Gu, H. Lin, Z. Huang, Q. Tang, X. You, C. Saggese, Y. Li, H. Jung, L. Deng, I. Wlokas, H. Wang, Mobility size and mass of nascent soot particles in a benchmark premixed ethylene flame, Combust. Flame 162 (2015) 3810–3822.
[43] H. Gao, H. Yu, Y. Tang, X. Yu, W. Zhang, L.T. DeLuca, R. Shen, Catalytic effects of transition metal oxides on HTPB-based fuel polymer matrices, FirePhysChem 5 (2025) 201–208.
[44] H. Arisawa, T.B. Brill, Flash pyrolysis of hydroxyl-terminated polybutadiene (HTPB) II: implications of the kinetics to combustion of organic polymers, Combust. Flame 106 (1996) 144–154.
[45] H. Arisawa, T.B. Brill, Flash pyrolysis of hydroxyl-terminated polybutadiene (HTPB) I: analysis and implications of the gaseous products, Combust. Flame 106 (1996) 131–143.
[46] B.T. Bojko, C.M. Geipel, B.T. Fisher, D.A. Kessler, Numerical sensitivity analysis of HTPB counterflow combustion using neural networks, Combust. Flame 271 (2025) 113829.
[47] M. Negri, H.K. Ciezki, Combustion of Gelled Propellants Containing Microsized and Nanosized Aluminum Particles, J. Propuls. Power 31 (2015) 400–407.
[48] A.K. Vasudevan, E. Hagen, Y. Zhou, K. Shi, L. Yang, M.R. Zachariah, In-situ growth of nanoaluminum in hydroxyl terminated polybutadiene and combustion characteristics, Fuel 407 (2026) 137273.